





Cite this: *New J. Chem.*, 2025, 49, 1982

In situ oxygen vacancy formation at the metal/TiO₂ interface during ammonia borane hydrolysis: a study of CuCo nanoparticles supported on various colored TiO₂ samples†

Dinabandhu Patra,^a Reeya Garg,^b Ankita Singh,^a Ujjal K. Gautam,^b Ramakrishnan Ganesan ^{*a} and Balaji Gopalan ^{*a}

The effects of *in situ* generated interfacial oxygen vacancies on the catalytic efficiency of copper–cobalt (CuCo) supported on colored TiO₂ nanoparticles were studied. These catalysts were synthesized *via* a solid-state approach and tested for their hydrogen generation efficacy during ammonia borane (AB) hydrolysis. The formation of *in situ* oxygen vacancies at the metal–TiO₂ interface is proposed. The *in situ* oxygen vacancies were studied by analyzing the rutile Raman band at 440 cm^{−1}, and the change in the intensity of the Raman band was related to the concentration of the generated oxygen vacancies. We conclude that white TiO₂ serves as a better support than reduced colored TiO₂.

Received 8th August 2024,
Accepted 3rd January 2025

DOI: 10.1039/d4nj03542a

rsc.li/njc

1. Introduction

The functionalities and catalytic efficiencies of many catalysts are determined by the defects present in their crystal structures.^{1–10} For example, TiO₂ is an important photocatalytic system in which defects impact catalytic efficiencies.^{11–17} The interest was also in understanding the catalytic nature of mixed TiO₂ phases^{18,19} and colored TiO₂ materials with tailored defect structures have been reported in the literature.^{20–22} Theoretical calculations play a crucial role in understanding the structural and electrical properties, as well as the surface modifications of different TiO₂ phases, and their influence on catalytic activity and environmental remediation.^{23–26} Black TiO₂ comprising a crystalline core and a nanometric disordered shell has been eliciting interest due to dramatically enhanced photocatalytic activities,^{15,27,28} and there have been studies on the role of defects in the catalytic characteristics.^{29–33} The photocatalytic activity of black TiO₂ has been attributed to the thin disordered surface layer that disrupts the bulk periodicity.^{32,34} The surface characteristics of black TiO₂ have been studied, and the consensus is that the surface is disordered/amorphous.^{33,35,36} It is

proposed that the oxygen vacancies are located at the sub-surface and are available for photocatalytic activity. One method of creating oxygen vacancies is by manipulating the interface between the oxide surface and the metal.^{37,38} The impact of defects in TiO₂ extends beyond catalytic applications to include semiconductor devices as well.³⁹ This interface depends on the relative amounts of the metal, synthesis procedure, and the characteristics of the underlying TiO₂. Despite these advancements, the understanding of the role of oxygen deficiency in TiO₂ when used as a support substrate is scarce.

On a different note, the hydrogen economy is poised to play a significant role in the next generation energy sector, thanks to the advancements in hydrogen generation strategies. However, certain obstinate challenges associated with the storage and transportation of this fuel warrant efficient catalysts to generate it in an on-demand fashion from easily transportable hydrogen sources/precursors like ammonia borane (AB). AB is a high hydrogen containing compound with 19.6% hydrogen by weight. Besides, it is lightweight, highly soluble in water under ambient conditions, and stable at room temperature.^{40,41} Although noble metal-based catalysts have been extensively studied towards this, due to their high cost and global reserve scarcity, it is essential to develop affordable catalysts based on non-precious earth-abundant metals.⁴² Although several works have been carried out in this regard, only a few transition metal-based catalysts have been reported that exhibit a turn-over frequency (TOF) greater than 50 min^{−1}.^{43,44}

With the above understanding, we pose two questions: (i) if the oxygen vacancies are located at the sub-surface, would exposing the surface to air eliminate the defects due to re-

^a Department of Chemistry, Birla Institute of Technology and Science – Pilani Hyderabad Campus, Jawahar Nagar, Kapra Mandal, Hyderabad – 500 078, India. E-mail: ram.ganesan@hyderabad.bits-pilani.ac.in, gbalaji@hyderabad.bits-pilani.ac.in

^b Department of Chemical Sciences, Indian Institute of Science Education and Research (IISER) – Mohali, SAS Nagar, Mohali, Punjab – 140306, India

† Electronic supplementary information (ESI) available: A video file is also available that shows the formation of intermediate dark color of the catalysts during the catalysis reaction. See DOI: <https://doi.org/10.1039/d4nj03542a>



oxidation? (ii) Would the re-oxidized surface layer respond to reducing conditions?

To answer the above questions, we produced discontinuous nanometric bimetallic islands of copper-cobalt (CuCo) on nanostructured TiO₂ by a solid-state synthetic approach and studied their catalytic activity in AB hydrolysis that generates hydrogen. Cu and Co metals exhibit good catalytic activity and synergy for H₂ generation reactions.⁴⁵ Here, we screened a series of CuCo mixed compositions and pure elements supported on TiO₂ nanoparticles and performed *in situ* Raman measurements to show the correlation between the formation of oxygen vacancies during the reaction and improvements in catalytic efficiencies.

2. Experimental section

2.1 Materials and sample preparation

The transition metal precursor cobalt(II) chloride hexahydrate (CoCl₂·6H₂O) was procured from SD Fine Chemicals, India and used as received. Copper(II) nitrate trihydrate (Cu(NO₃)₂·3H₂O), copper (<425 μm, 99.5% metals), and cobalt (2 μm, 99.8% metals) powders, and TiO₂ nanopowder (<100 nm, catalog #634662) were purchased from MilliporeSigma. The reagents sodium borohydride (NaBH₄), ammonium sulfate (NH₄)₂SO₄, and tetrahydrofuran (THF) were procured from SRL Chemicals Pvt. Ltd, India. Ammonia borane was synthesized following a literature protocol.⁴⁶ Milli-Q water was used throughout the work.

In a typical synthesis, a calculated amount of the dry Co or Cu precursor was ground well in a mortar for 5 minutes. The exact amounts of the precursors used are given in Table S1 (ESI[†]). About 200 mg of TiO₂ nanopowder along with 15 μL of water was added to the mortar and the grinding was performed for another 5 minutes. The obtained mixture was then dried at 70 °C for 15 min, followed by the addition of 10 equivalents of solid sodium borohydride with respect to the transition metal and further grinding for about 5 minutes. The resultant product was washed twice with 30 mL of water and then with 15 mL of ethanol and finally dried in air. The samples are coded as M-x, where M represents the white TiO₂@CuCo and x represents the loading of the CuCo expressed in weight percentage of metals. The percentages of metals were determined by X-ray fluorescence (XRF). Prior to determining the elemental weight percentages for the samples, a calibration curve was prepared using samples mixed with known quantities of commercial metallic copper, cobalt, and TiO₂. The metal content in the catalysts after the synthesis process was determined from the calibration graph. In the M-x series, the ratio of Cu:Co was 1:1 which is as per the initial metal feed ratio. The samples G-M-3 and C-M-3 represent grey-TiO₂ and charcoal-TiO₂ based samples, respectively. Colored TiO₂ samples were synthesized by following a literature report.²² In brief, 1 g commercial TiO₂ was mixed with 325 mg sodium borohydride in a mortar, then calcined at 300 °C in a tubular furnace under an argon atmosphere for 30 and 60 min to obtain grey-TiO₂ and charcoal grey-TiO₂, respectively. Fig. S1 (ESI[†]) shows the digital pictures of the colored TiO₂

powders. After the reaction time, the furnace was cooled normally. The sample code M(y:z)-3 means y and z are the weight ratios of Cu to Co (as per the initial feed weight ratio) for the total metal content of 3% by weight.

2.2 Characterization methods

High resolution transmission electron microscopy (HR-TEM) images of the samples were collected using a JEOL JEM-F200. X-ray diffraction (XRD) measurements were performed for all the samples in the two-theta range from 20° to 80° at a step size of 0.01 and a 1° min⁻¹ scan rate using a Rigaku Ultima IV X-ray diffractometer and a Cu-Kα source. SAXS measurements were performed using the same XRD instrument. The measurements were made using the $2\theta\left(q = \frac{4\pi\sin\theta}{\lambda}\right)$ value of 0.06° to 2° at a scanning speed of 0.03° min⁻¹. The sample was placed and spread over a scotch tape and data were recorded in transmission geometry. For all the samples, the results are presented after due background subtraction. The data were analyzed using the NANO-Solver software provided by the instrument manufacturer. The weight percentages of all metals present in the samples were confirmed by XRF (Panalytical Epsilon-1). The core level X-ray photoelectron spectroscopy (XPS) was performed using a Thermo Fisher K-Alpha furnished with a monochromatic Al Kα X-ray source ($h\nu = 1486.6$ eV) and a dual beam flood gun to identify the chemical states of the elements present in the sample. Solid-state diffuse reflectance spectroscopy (DRS) measurements were conducted from 200 to 1000 nm at a scan speed of 400 nm min⁻¹ with a barium sulphate window as a reference using a JASCO V-670. The band gap values were determined from the intersection point of the two tangents in the Kubelka-Munk plot. The room temperature electron paramagnetic resonance (EPR) studies were carried out using an X-band Bruker Magnettech ESR 5000 instrument under 5 mW power and magnetic field scan between 320 mT and 350 mT in 60 s with twenty accumulations. Brunauer-Emmett-Teller (BET) surface area measurements were performed by using a Microtrac Bel BELSORP MINI II. The samples were degassed at 120 °C for 2 h under a nitrogen atmosphere before surface area measurements. Raman spectroscopy measurements were performed using a UniRAM-3300 Micro Raman Mapping Spectrometer. All the experiments were performed at 50× air-immersion objective with a laser power, an excitation wavelength, and an exposure time of 10% (<0.5 mW), 532 nm, and 1 s, respectively. A 100× objective was used to measure the Raman spectra at the end of the reaction. The rutile (440 cm⁻¹) to anatase (396 cm⁻¹) peak area ratio was calculated employing Fityk-curve fitting and peak fitting software using pseudo-Voigt profiles. For M-x samples, the ratio changed with power; besides the formation of a new Raman band was also observed.

2.3 Catalytic hydrolysis of AB

For hydrogen generation experiments, 50 mg catalyst was dispersed in 13 mL of water in a 25 mL two-necked round-bottom flask. The bottom of the flask was partially immersed in



a water bath of a mild ultrasonicator (Bio-Technics, India, 230 V AC 50 Hz). One neck of the flask was connected with a water-filled inverted burette, while the other neck was closed with a rubber septum. About 2 mL of aqueous solution containing 1 mmol (30.8 mg) of AB was injected into the reaction solution under sonication, and the amount of H₂ gas generated was monitored by water displacement in the burette. The entire experiment was performed at room temperature. After every cycle of hydrogen generation, the catalyst was collected by centrifugation of the solution. The next cycle was performed by adding a fresh aqueous ammonia borane solution. Further cycles were performed at 5 min intervals.

The TOF of the catalysts was calculated from the equation:

$$\text{TOF} = \frac{3 \times \text{moles of ammonia borane}}{\text{moles of the transition metal catalyst(s)} \times \text{time}}$$

2.4 In situ Raman experiments

For the *in situ* Raman experiments, we mixed the catalyst and AB, and the mixture was placed on a glass slide and smeared. Then, a little amount of water was added using a micropipette on the periphery of the solid mixture, thereby allowing water to seep through the catalyst. The Raman spectra (during the catalysis reaction) were recorded in the water seeped region (at the time of measurement, the catalyst appeared darkish when compared to its initial color). More water was added to the darkish region and the spectra (after catalysis) were recorded again at the same spot. The intensity ratio did not change with magnification and power for commercial TiO₂ under the experimental conditions.

3. Results and discussion

Transition metal nanostructures were prepared by aqueous reduction of metal salts using sodium borohydride.⁴⁷ On the other hand, Hutchings *et al.* reported the synthesis of supported Au nanoclusters by solid-state mixing of precursors with the support followed by heat treatment.⁴⁸ Pradeep *et al.* and Jagirdar *et al.* used solid sodium borohydride to prepare atom-precise Ag nanoclusters and noble metal nanoclusters, respectively.^{49,50} In our work, a solid-state synthetic approach that combines the above methods was employed to prepare the catalysts. We have employed a solid-state method for the synthesis of white-TiO₂ supported monometallic and bimetallic systems. However, only the CuCo based bimetallic system will be discussed for reasons that will be evident later in this paper. The samples are coded as M-*x* where M denotes a 1:1 alloy of Cu and Co unless otherwise specified, while *x* is the wt% of the CuCo alloy on the TiO₂ support structure. The catalysts with 3 wt% CuCo on commercial TiO₂ nanostructures with variable ratios of Cu and Co are referred to as M(*y*:*z*)-3. Catalysts containing 3 wt% of CuCo (1:1) supported on grey- and charcoal grey-TiO₂ are labelled as G-M-3 and C-M-3, respectively. Table S2 (ESI†) presents the chemical compositions of various catalysts based on their feed ratios and post-synthesis determined by XRF. In general, the trend in the molar ratio between Cu and Co aligned with that of the feed ratio, though the loading of Cu in the final composition was found to be slightly lower. This could be

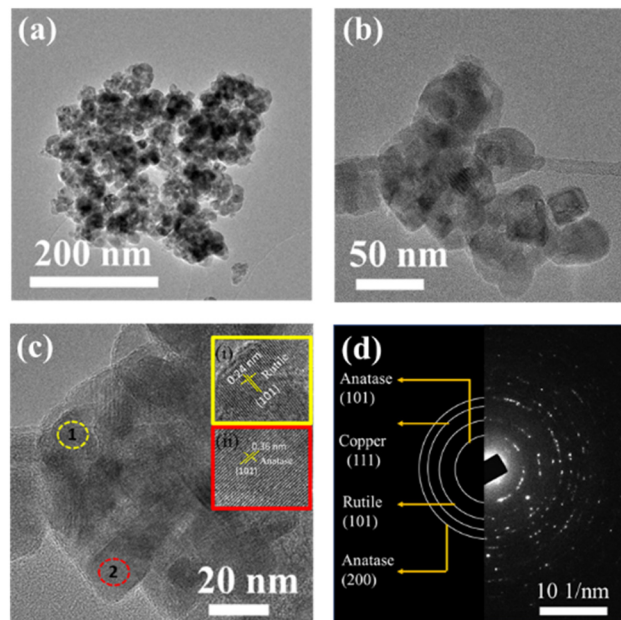


Fig. 1 (a) and (b) Low-magnification TEM images and (c) HRTEM image of the M-3 sample. Inset images (i) and (ii) in (c) highlight the selected regions of the sample showing lattice fringes corresponding to the rutile and anatase phases of TiO₂ (labelled with boxes 1 and 2). (d) Typical SAED pattern of the sample.

attributed to the leaching of a small amount of Cu from the surface of TiO₂ nanoparticles, which was not the case with Co. Fig. S2 (ESI†) shows the SEM-EDX elemental mapping for M-10 and M(1:4)-3. It can be observed that both Co and Cu are uniformly dispersed everywhere in the M-10 catalyst, and for the M(1:4)-3 catalyst, Cu is less than Co as the feed ratio of Cu to Co was 1:4. Nevertheless, we will continue to refer to the catalysts according to their feed ratios. Fig. 1 shows the high-resolution transmission electron microscopy (HRTEM) images of M-3, which revealed lattice fringes of 0.36 and 0.24 nm corresponding to the (101) planes of anatase and rutile phases, respectively. Neither discrete Cu nor Co particles in the TEM images were observed, and there were no strong diffraction peaks in the XRD pattern. We assume that their sizes are rather small and, therefore, form a good dispersion on the surface of TiO₂. Similar observations were made in other samples as well, which confirmed that metal loading does not change the TiO₂ morphology (Fig. S3–S5, ESI†). Another set of lattice fringes measuring 0.21 nm was occasionally observed (Fig. S4 and its inset, ESI†), which may be assigned to either the (111) plane of Cu (0.215 nm) or Co (0.204 nm). The presence of Cu/Co was confirmed by the presence of the (111) peaks in the selected area electron diffraction (SAED) patterns of all the samples (Fig. 1(d) and Fig. S3–S5, ESI†).

The XRD patterns of the synthesized samples were the same as that of commercial TiO₂ (Fig. 2), consisting of anatase (JCPDS # 84-1286) and rutile (JCPDS # 88-1175) phases. The percentage of the rutile phase in the mixture was determined (using HighScore™) to be 10%. The grey and black TiO₂ were also found to have a similar composition to white TiO₂. As the grey and black TiO₂ samples were formed by the reduction of



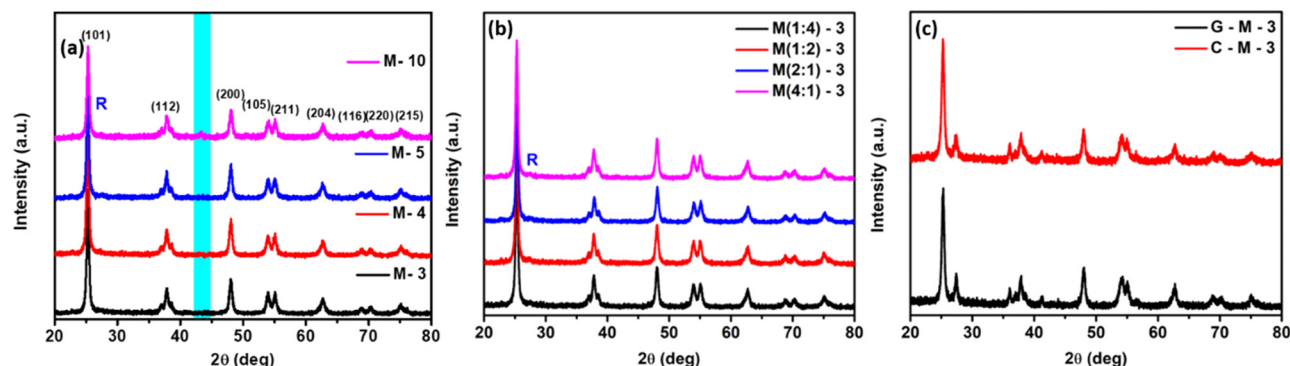


Fig. 2 XRD patterns of all synthesized (a) M-*x*, (b) M(*y*:*z*)-3, and (c) G-M-3 and C-M-3 samples. The peak at $2\theta = 43.3^\circ$ corresponds to metallic copper (shaded area).

white TiO_2 , it is most likely that the oxygen vacancies were created at the surface. Hence, we presume that the structure of grey and black TiO_2 has an oxygen-deficient coating at the surface and can be expressed as $\text{TiO}_2@\text{TiO}_{2-x}$. Since the creation of oxygen vacancies has not impacted the crystalline structure and composition, the surface TiO_{2-x} is considered to be amorphous. For M-3, M-4 and M-5 samples, the pattern looked similar to that of commercial TiO_2 . For M-10 (Fig. 2a), in addition to the characteristic peaks of TiO_2 (no change in the percentage of rutile phase was observed), two small peaks at 43.3° and 50.4° corresponding to the (111) and (200) planes of the fcc metallic copper were observed (JCPDS # 04-0836). This result showed the successful reduction of Cu^{2+} to Cu^0 over the TiO_2 support. The 2θ values for Cu^0 also indicated that the synthesized catalysts were bimetallic contact aggregates in nature. The absence of Co metallic or oxide forms (due to aerial oxidation) in these catalysts could be attributed to the high dispersion and/or amorphous nature of the Co and its oxides. In M(*y*:*z*)-3 samples, TiO_2 peaks were observed with no signatures of Cu and Co components (Fig. 2b). For grey- TiO_2 and charcoal grey- TiO_2 , the XRD features remained intact, including rutile percentage and crystallite size. The TiO_2 crystallite size did not change and was ~ 18 nm (Fig. 2c). The small-angle X-ray scattering (SAXS) pattern remained unchanged, indicating that the physical attributes of TiO_2 did not change due to reduction (Fig. S6, ESI†). The SAXS data were fitted with a spherical model and the particle size of various TiO_2 samples was ~ 20 nm. The particle size distribution also did not change (Table S3, ESI†). The SAXS patterns of the normal M(1:4)-3 sample are given in Fig. S7 (ESI†) and the corresponding fit parameters are tabulated considering the TiO_2 core-metal shell model in Table S3 (ESI†). A shell size of 0.1 nm was obtained; however, the particle size did not change appreciably during the catalyst synthesis. However, with a scattering intensity-based analysis, a higher intensity observed for the M(1:4)-3 sample compared to commercial TiO_2 at all “*q*” values indicates the metal dispersion over the TiO_2 . In general, the scattering intensity depends on the number of electrons and it increases with increasing atomic number of the scatterer. Thus, only the presence of a metallic shell (Co and Cu) over TiO_2 could enhance the scattering intensity. Such variation of the SAXS intensity of the Fe_3O_4 core due to shell metals has been reported in $\text{Fe}_3\text{O}_4@\text{Au}$ and

$\text{Fe}_3\text{O}_4@\text{Ag}$ core-shell nanostructures.⁵¹ For G-M-3 and C-M-3 samples, the XRD patterns were dominated by the pattern of commercial TiO_2 . ED-XRF was employed for determining the metal loading over TiO_2 . Peaks at 4.5 and 4.9 keV are due to Ti K_α and Ti K_β , while those at 6.9, 7.6, 8.0, and 8.9 keV correspond to Co K_α , Co K_β , Cu K_α , and Cu K_β , respectively. The elemental compositions of the final samples and their feed ratios are given in Table S2 (ESI†).

The Ti 2p edge spectra (measured without sputtering) in the X-ray photoelectron spectroscopy (XPS) were observed to be broadened due to the presence of Ti^{3+} . From M-3 to M-10 (Fig. 3a), the peak broadening increased and the peak shifted towards lower binding energies than normal TiO_2 . For C-M-3 and G-M-3 samples, both the peak shift and broadening were more than those for M-*x* samples. At the Ti-edge, there was a peak shift for G-M-3 and C-M-3 by 0.6 and 0.4 eV, respectively. And for M-10, the peak shift was 0.2 eV. The peak has shifted slowly from M-3 to M-10 towards lower binding energies.

At the Cu edge (Fig. S8b–d, ESI†), for M-10, the deconvolution of the Cu 2p_{3/2} peak revealed two features at 932.4 eV and 933.8 eV, due to the presence of Cu^0 and Cu^{2+} , respectively. The satellite peaks for Cu^{2+} at 943.8 eV and 962.5 eV were also observed.⁵² Except for a thin oxide layer at the surface and at the copper- TiO_2 interface, copper was in the metallic state, which agrees with the XRD data. At the Co edge in M-10 samples, where both Co^{2+} at 780.7 eV with a satellite peak at 786.6 and a small amount of metallic cobalt peak at 778.2 eV were present. The presence of the dominant oxidized form of Co is due to aerial oxidation. For the O edge (Fig. S8b, ESI†), broadening was observed as before, suggesting the presence of more than one type of oxygen species, which is oxygen vacancy. The relative amount of oxygen vacancies was found to increase with increasing metal loading. The metal ratio was also obtained from XPS, and the values are 0.61, 0.6, 0.59, and 0.72 for M-3, M-4, M-5, and M-10, respectively. This indicates more Co is present at the surface. For M(*y*:*z*)-3 samples, the ratio was 0.17, 0.3, 1.04 and 8.29 for M(1:4), (1:2), M(2:1) and M(4:1), respectively, indicating that more Co is present at the surface with increasing Co feed content. At the O edge, the line broadening increased with G-M-3 and C-M-3 samples. The spectra of the M(*y*:*z*)-3 samples looked similar to those of the other samples, except for higher Co^0 intensity in Co-rich samples (Fig. S9, ESI†).



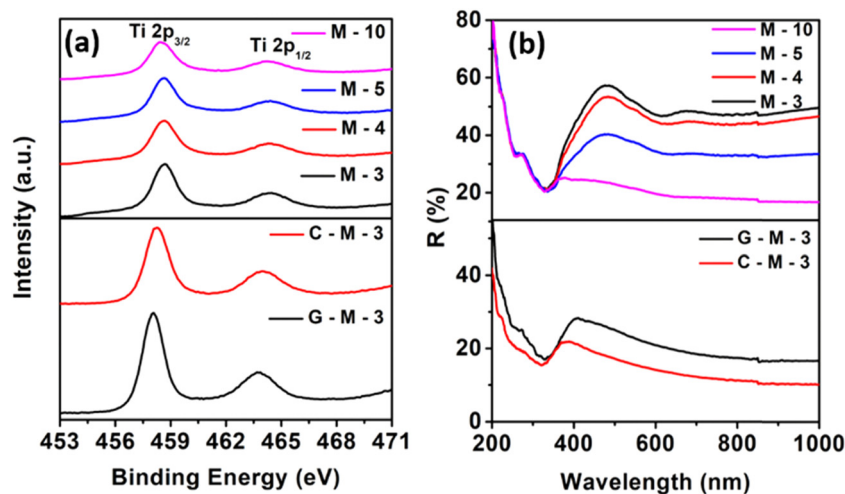


Fig. 3 (a) Ti 2p edge narrow scan and (b) solid-state DRS spectra of the catalysts.

Solid-state diffuse reflectance spectroscopy (DRS) (Fig. 3b) of commercial TiO_2 showed low reflectance in the entire UV region but high reflectance in the visible light region. In the case of M-x samples, there was high absorbance in the visible light range along with the characteristic TiO_2 absorbance patterns. At wavelengths > 400 nm, the reflectivity decreased, and the bandgap remained constant around 3.3 eV with an increase in bimetallic loading (Fig. S10, ESI[†]). This indicated that the metals were well-dispersed on the surface of the TiO_2 nanoparticles and the decrease in the reflectivity can be attributed to the presence of oxygen vacancies at the TiO_2 and bimetal interface at the surface. It is worth noting that the reflectivity was higher in the visible region for the samples prepared by simply mixing Co^{2+} and Cu^{2+} salts with commercial TiO_2 , which is different from the spectra of catalyst samples. This indicates the presence of Co and Cu in their elemental state due to reduction by sodium borohydride during the synthesis. There is no shift in the band gap in the G-M-3 and C-M-3 samples; however, the reflectivity decreased from M-3 $<$ G-M-3 and C-M-3 samples. The spectral features were found to be dependent on the composition (Fig. S11a, ESI[†]). For M(y : z)-3, the reflectivity was found to depend on the Co content. On the other hand, the decrease in reflectivity was also observed in colored- TiO_2 samples (Fig. S11b, ESI[†]). Thus, the similar nature of surface in colored TiO_2 and metal-supported commercial TiO_2 is revealed.

Fig. S12 (ESI[†]) shows the merged EPR spectra of white TiO_2 , M(1 : 4)-3, and M10 catalysts. A peak in the EPR spectrum ($g = 2.005$) indicates the presence of oxygen vacancies, arising from the paramagnetic centers associated with Ti^{3+} ions.^{11,14} As all the spectra were recorded under identical instrumental conditions and amount, the difference in the intensity indicates the difference in the amount of oxygen vacancies present in the samples. The sample M-10 has the highest number of oxygen vacancies among the three measured samples due to higher metal content. This supports our hypothesis (in this study) and corroborates the DRS data.

The surface area values obtained from the BET studies for the various catalyst compositions are summarized in Table S5 (ESI[†]). It can be seen from the table that the surface area of the pristine TiO_2 support was found to be $64 \text{ m}^2 \text{ g}^{-1}$. The surface area of grey- TiO_2 and charcoal grey- TiO_2 was 60 and $51 \text{ m}^2 \text{ g}^{-1}$, respectively. The surface area was not affected when the different colored TiO_2 was loaded with 3% CuCo. The surface area decreased with increasing the bimetallic loading to $55 \text{ m}^2 \text{ g}^{-1}$ for M-5, but the value increased to $71 \text{ m}^2 \text{ g}^{-1}$ for M-10. Nevertheless, the surface area of all the catalysts supported over TiO_2 can be deemed to be in a closer range for practical purposes.

The time required for the catalysts to produce the maximum amount of hydrogen was found to be in the order $\text{TiO}_2\text{-Cu-10} > \text{TiO}_2\text{-Ni-10} > \text{TiO}_2\text{-Co-10}$. All the catalysts exhibited an induction period in the first two cycles. Therefore, the TOF values are reported for the third cycle. The TOF values of the Fe, Cu, Ni and Co monometallic catalysts were found to be 12.1, 16, and 20.2 min^{-1} , respectively. The supported Fe catalyst was found to be inactive and such observations have been reported earlier.⁵³ The TOF values of the CuFe, FeNi, CoNi, CuNi and CuCo bimetallic catalysts obtained in the third cycle were found to be 7.1, 13.2, 14.2, 17.2 and 55 min^{-1} , respectively. Since CuCo bimetallic catalysts were more active, we studied these systems in detail. The catalytic efficiencies of the as-synthesized M-x catalysts on AB hydrolysis were then investigated. The TOF values for M-3, M-4, M-5, and M-10 were 66.7, 66.3, 61.1, and 55.0 min^{-1} , respectively (Fig. 4a). The TOF decreased with an increase in catalyst content beyond 4 wt%. In catalytic hydrolysis using M(4 : 1)-3 (Fig. S13, ESI[†]), the TOF was 49.3 min^{-1} during the third cycle. With an increase in cobalt loading, the TOF was found to increase and the catalyst M(1 : 4)-3 exhibited the highest activity. The plausible reason for this observation is explained as follows. Metallic copper grows quickly due to its higher diffusion coefficient compared to cobalt. This was confirmed by the appearance of the Cu(111) diffraction peak when the copper loading in the catalyst increased, a phenomenon not observed with increased cobalt loading. In the current study, metallic copper



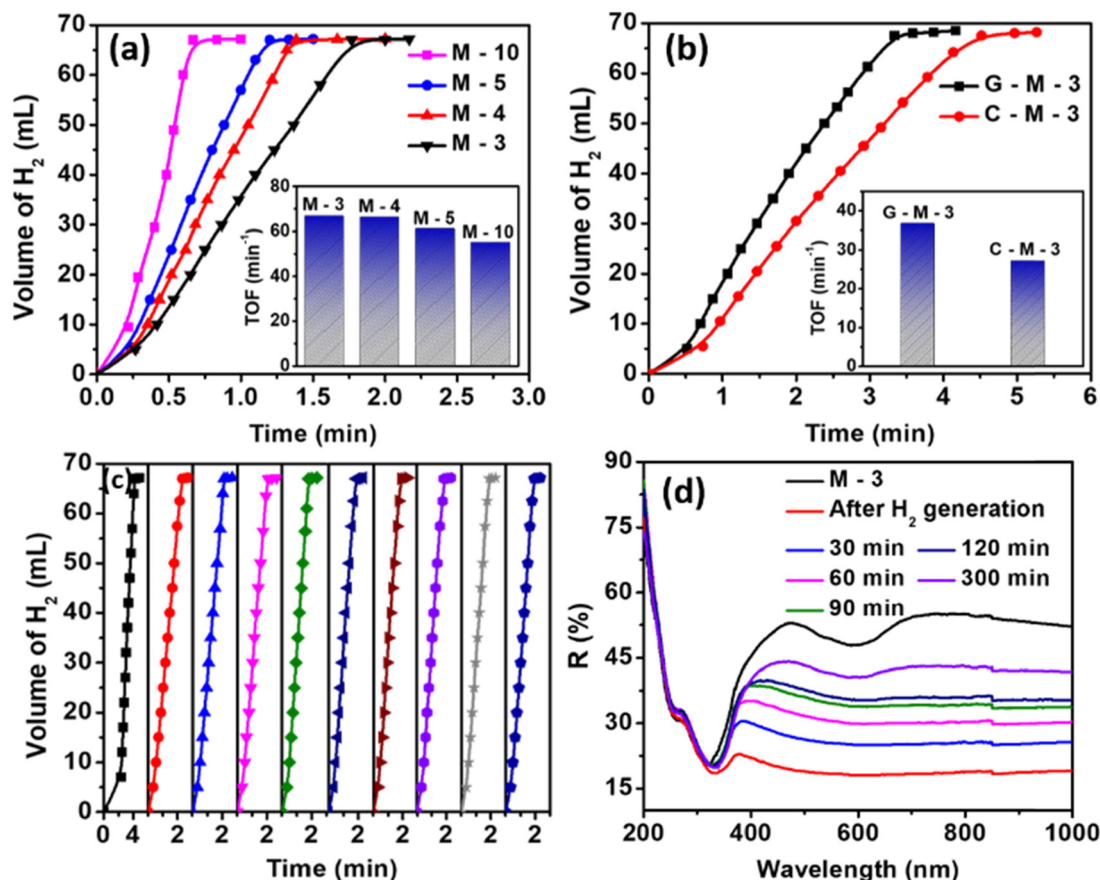


Fig. 4 Catalytic hydrogen generation from the hydrolysis of ammonia borane with (a) M-x, (b) G-M-3, and C-M-3 catalysts; insets show the corresponding turnover frequencies; (c) hydrogen generation recyclability with the M(1:4)-3 sample; and (d) solid-state DRS spectra of the M-3 sample measured every 30 min after reaction completion.

grew faster, forming larger particles, which resulted in copper leaching due to a decreased metal-support interface area. Consequently, as copper leaching increased, the hydrogen generation reaction rate decreased. In contrast, cobalt leaching was minimal or nonexistent due to the strong Co-TiO₂ interface, resulting in an increased reaction rate with higher cobalt loading. In earlier reports, Co-rich samples exhibited better catalytic activity than the Cu-rich samples with TiO₂ as a support in H₂ generation from AB.^{54–57}

A comparison of the catalytic efficacy of bimetallic transition metal catalysts anchored over various supports is presented in Fig. 4b. The G-M-3 and C-M-3 catalysts showed TOF values of 36.7 and 27.3 min⁻¹, respectively; the trend in activity was M-3 > G-M-3 > C-M-3. A maximum TOF value of 69.2 min⁻¹ was recorded in the fourth cycle for M(1:4)-3, which was preserved until the tenth cycle (Fig. 4c), indicating good catalytic stability. The TOF value at every cycle was calculated and is presented in Table S6 (ESI[†]). For M-10, the TOF remained constant (55 min⁻¹) up to the fifth cycle. The kinetics and thermodynamics studies are presented in Fig. S14 (ESI[†]).

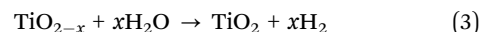
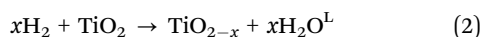
The initial color of M-3, M-4, and M-5 was dirty white. Upon adding AB into the reaction medium, the catalyst turned dark, after which the reaction rate increased rapidly. Since M-10 was initially dark in color, the color change during the hydrogen

generation reaction was unclear. This observation indicates the *in situ* formation of dark TiO₂.^{28,58} However, the dark color disappeared slowly after AB was consumed completely and the catalyst returned to its original color. Upon exposure to air, it took a long time for the DRS spectra of the recovered catalyst to match with those of the fresh sample. The DRS study was carried out using the M-3 (optimal) catalyst after recovery from the solution (Fig. 4d). After 30 min, the absorbance of the recovered catalyst was found to slightly decrease, indicating the regeneration of the original TiO₂ support. We propose that the intermediate dark color is due to reactive oxygen vacancies at the metal-TiO₂ interface and that their presence promotes H₂ generation rate. The number of vacancies increases during the reaction, and vacancies are continuously generated during the AB hydrolysis reaction.

In general, the absolute quantification of oxygen vacancies is difficult. Instrumental techniques like DRS, electron spin resonance (ESR) spectroscopy, X-ray absorption near edge structure (XANES), XPS, and Raman spectroscopy are some of the commonly employed ones.^{11,59} However, in the context of the current study, the transient nature of the oxygen vacancy in the catalysts is responsible for the high catalytic activity. The transient oxygen vacancy then gets re-oxidized upon exposure to the atmospheric oxygen after the reaction, which increases



the complexity of stabilizing and probing the same. DRS can be used if the component is a semi-conductor, and hence we employed the same and observed a clear decrease in the percentage reflectance soon after the reaction, wherein the spectral profile qualitatively indicated the formation of oxygen vacancies in TiO_2 (Fig. 4). The DRS spectral profile was found to return to the initial state due to re-oxidation. Apart from this, indirect evidence for oxygen vacancies can be provided through IR spectroscopy, Raman spectroscopy and XPS using line broadening. Besides, we note that the number of vacancies formed during the synthesis of the samples does not affect the AB hydrolysis. But the ability to generate *in situ* oxygen vacancies plays an important role. We have observed that the TOF is dependent on the nature of the TiO_2 support for a fixed metal content and composition. The TiO_2 undergoes a change during the reaction, which is evident from the Raman spectrum and DRS data of the used catalysts. While we propose that oxygen vacancies activate the water, the lattice oxygen from TiO_2 is also consumed. It is important to note that (1) bare TiO_2 does not catalyze the AB hydrolysis reaction, and (2) metal centers are the active catalysts.



where the superscript "L" indicates the lattice oxygen. The water activation step (eqn (3)) occurs at both metal and metal- TiO_2 interfaces. The oxidation of TiO_{2-x} is fast if the catalysts were exposed to air. Even the well-known ceria in catalytic converters reacts first, but then gets regenerated later.^{60,61}

Raman spectroscopy is generally used to study the presence of anatase and rutile phases in TiO_2 , including in the colored forms.⁶² Colored TiO_2 has been produced by reducing white or normal TiO_2 samples.^{22,29,63} In our samples, the Raman bands were similar to those of the reported values for P25.⁶⁴ The Raman bands assigned for anatase are as follows: E_g (144 cm^{-1}), E_g (196 cm^{-1}), B_{1g} (396 cm^{-1}), ($A_{1g} + B_{1g}$) (518 cm^{-1}), and E_g (636 cm^{-1}), and for rutile: E_g (440 cm^{-1}) and A_{1g} (610 cm^{-1}). We inferred from the earlier reported Raman data that the intensity of the 440 cm^{-1} band may be correlated to the color of TiO_2 (*i.e.*, decreases with the degree of reduction). Our study also showed a drop in the intensity of the 440 cm^{-1} band (rutile E_g) with the degree of reduction (Fig. 5a). The rutile E_g band is related to Ti-O bonds and any decrease in the intensity of E_g signifies a change in the Ti-O bond. The decrease in the intensity may also be due to the broadening of the band leading to an overlap with the 396 cm^{-1} (B_{1g}) anatase band. Thus, the ratio of the intensity of 440 cm^{-1} and 396 cm^{-1}

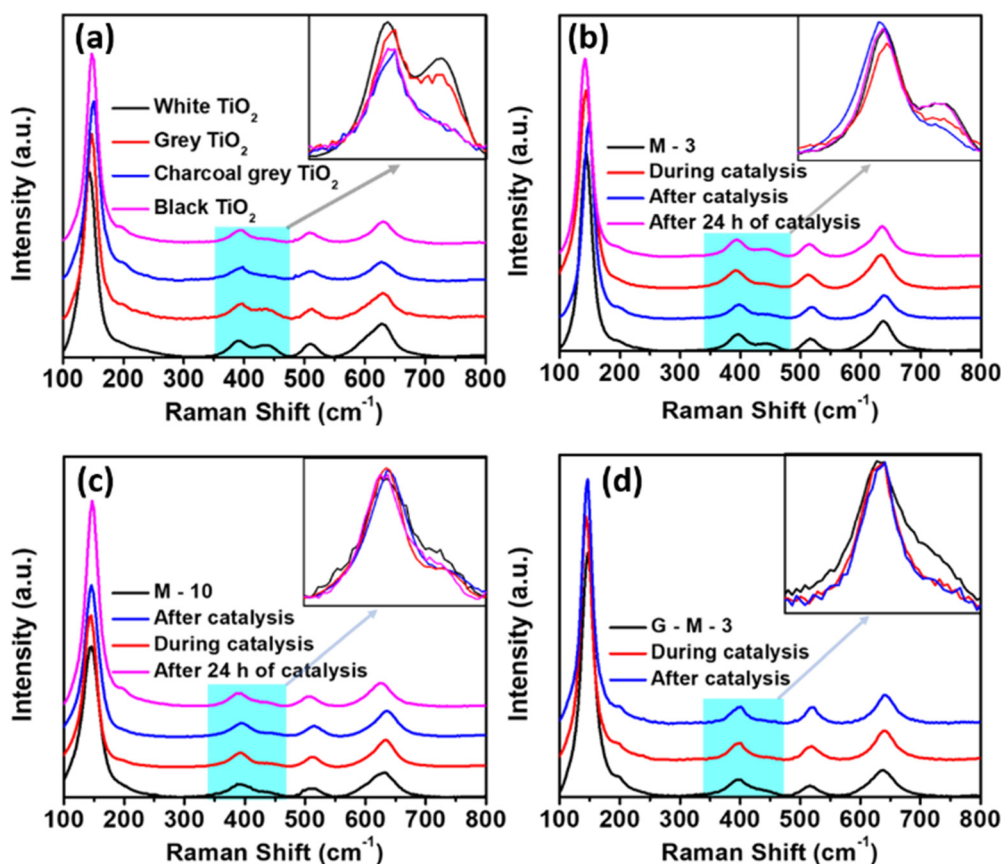


Fig. 5 (a) Raman spectra of various colored TiO_2 samples; *in situ* Raman spectra of (b) M-3, (c) M-10, and (d) G-M-3 samples. Inset: The intensity was normalized to the peak value.



bands can be used to study the relative change in oxygen vacancies. The ratios of the intensities of the 440 cm^{-1} and 396 cm^{-1} bands were 0.68, 0.56, 0.13, and 0.09 for white, grey, charcoal grey, and black TiO_2 , respectively. Interestingly, the intensity of the band at 440 cm^{-1} corresponding to rutile decreased with increasing metal loading and the ratios were 0.35 and 0.13 for M-3 and M-10 samples, respectively. The changes in the Raman peak area ratio for different catalysts are summarized in Tables S7–S9 (ESI[†]).

We propose that the rutile phase acts as the nucleation center for the metals. Both metals and oxygen vacancies are located here, *i.e.*, oxygen vacancies are located at the metal and metal oxide interfaces. Fig. 5b shows the Raman spectra of the M-3 catalyst; it can be seen that the intensity of the 440 cm^{-1} band decreased during the reaction. On exposure to air, the intensity increased again due to re-oxidation. In M-10 (Fig. 5c), there were two salient features: (1) the extent of intensity reduction of the Raman band was small, and (2) the time taken for re-oxidation was large, unlike for M-3. Therefore, the relative change in the intensity of the 440 cm^{-1} band signifies the relative concentration of *in situ* oxygen vacancies formed during the H_2 generation reaction. The rate of H_2 production was dependent on the number of O_2 vacancies produced *in situ*.

The changes in the intensity of the 440 cm^{-1} Raman bands in M-3, G-M-3 (Fig. 5d), and M-10 were 49%, 45%, and 36%, respectively. It should be noted that, for M-3 and G-M-3 samples, the catalyst parameters like the surface area, metal loading and catalyst loading were similar and thus the catalytic activity can be compared directly to the change in the intensity of the Raman band. Therefore, M-3 was more active than the G-M-3 and C-M-3 catalysts. This indicates that the *in situ* oxygen vacancies are more reactive than the already existing oxygen vacancies created during the synthesis step. The amount of oxygen vacancies created is proportional to the amount of oxygen available during the reaction. As the commercial TiO_2 is rich in oxygen, it serves as a better support. The higher activity of M-10 over G-M-3 and C-M-3 is due to a higher metal content. And the TOF of M-3 compared to the existing literature for non-noble metal-based AB hydrolysis also indicates that CuCo supported by white TiO_2 prepared by a solid-state approach shows a high activity (Table 1). The TOF values shown in Table 1 were calculated at the end of the hydrogen generation. Furthermore, the dark color was also observed while using sodium borohydride as the hydrogen source. Thus, the color is not due to any ammonia- $\text{Co}^{2+}/\text{Cu}^{2+}$ complex, as the complex formed between a transition metal ion and amine groups is generally blue in color. Besides, cobalt has a tendency to oxidize and, therefore, would exist as CoO , which upon reduction by AB may form Co , imparting a dark color. We observed the dark color in pure Cu based catalysts as well in which Cu exists as $\text{Cu}(0)$ as ascertained from XRD and XPS. The SAXS pattern of the used M(1:4)-3 catalyst is similar (Fig. S7, ESI[†]) to that of the fresh catalyst and the fitting parameters are given in Table S4 (ESI[†]). The physical attributes of particles did not change after the H_2 generation reaction. Thus, the dark color is not due to metal formation during the H_2 generation reaction. In order to show the applicability of these results, we performed the characterization and catalysis reaction of $\text{TiO}_2@\text{Cu-5}$ samples (Fig. 6). The observations

Table 1 Catalytic activity in AB hydrolysis with CuCo based catalysts

Sample	TOF (min^{-1})	Ref.
CuCo@MIL-101 (30:70)	19.6	49
CuCo/C (49:51)	45	65
CuCoO-GO (80:20)	70	66
CuCo/MCM-41 (20:80)	15	67
CuCo (48:52)	3.4	68
CuCo/g- C_3N_4 (7:93) (dark)	34.8	55
CuCo/g- C_3N_4 (7:93) (light)	75.1	55
CuCo/HPC (20:80)	19.1	54
CuCo/PDA-rGO (20:80)	51.5	69
CuCo/rGO (91:9)	9.1	70
CuCo@ SiO_2 (50:50)	5.3	67
$(\text{CuCo})_2/\text{Al-cat}$ (50:50)	2.7	71
CuCo/ TiO_2 (20:80)	69.2	This work

are similar to CuCo systems, including the *in situ* Raman characterization, in which the intensity of the 440 cm^{-1} band decreased during the reaction and increased when subjected to re-oxidation in air. In the initial cycle of hydrogen generation, there was a 2-minute induction period, which was not observed in subsequent cycles. This induction period is attributed to the reduction of TiO_2 and surface oxidized metals to metal nanoparticles. Since the metal oxides are only present on the surface of the Cu and Co metallic nanoparticles, it is expected that this layer would be reduced in the first cycle. In subsequent cycles, there is no induction period and the rate of hydrogen generation continued to increase up to the fifth cycle. These two observations are attributed to the reduction of the TiO_2 layer in each cycle, thus enhancing the hydrogen generation rate. This is further supported by the catalyst turning black during hydrogen generation. The hydrogen generation cyclability with the M(1:4)-3 catalyst and the hydrogen generation using the $\text{TiO}_2@\text{Cu-5}$ catalyst suggest that the black color formation during hydrogen generation is due to the reduction of TiO_2 at the metal- TiO_2 interface, rather than the surface reduction of metal oxides.

The hydrogen dissociation from water and AB occurs at the metal sites. The TiO_2 in the vicinity of the metal is reduced, thereby creating *in situ* vacancies during the reaction. The oxygen vacancies thus created are reactive and have an affinity towards oxygen, thereby activating the H_2O molecules.^{64,72–74} For instance, it has been reported that oxygen vacancies activate water on the surface of Co_3O_4 nanocrystals.⁷⁵ The unusually high reactivity of oxygen vacancies is because these are formed at the surface and activate water before it can diffuse into the sub-surface. The activity of CuCo coated black TiO_2 is indeed less than that of the normal TiO_2 supported CuCo system. Thus, it can be understood that the reaction involves metal-support interaction. The Co-rich samples are better catalysts because the rate of hydrogen generation from the AB is higher for the Co rich sample than Cu-rich based samples. This, in turn, generates more *in situ* vacancies, leading to more activation of water. Thus, on increasing cobalt content, the TOF increases.

The re-oxidation seemed to depend on the nature of the support and the metal content. For commercial TiO_2 and low metal content, re-oxidation was faster and easier. *In situ* dark TiO_2 is different from stable black TiO_2 because the Raman band at 440 cm^{-1} was not observed at all in the latter and could not be reversed. However, in the *in situ* dark TiO_2 , the intensity of



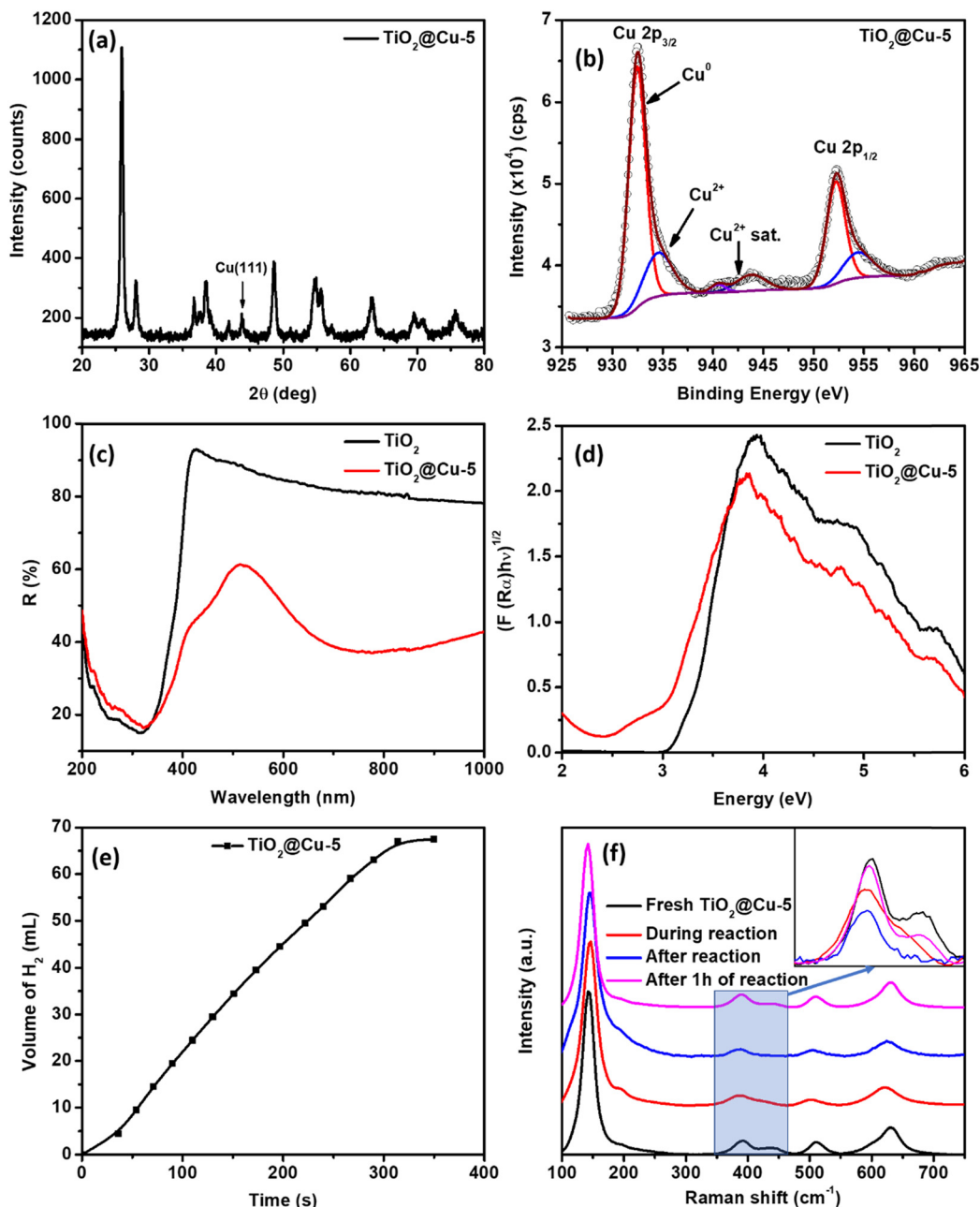


Fig. 6 (a) XRD pattern, (b) Cu narrow scan XPS spectra, (c) DRS spectra, and (d) the corresponding Kubelka–Munk plot for $\text{TiO}_2\text{@Cu-5}$. The DRS data were also compared with pure TiO_2 . (e) H_2 generation from AB hydrolysis with the $\text{TiO}_2\text{@Cu-5}$ catalyst. (f) *In situ* Raman spectra of the $\text{TiO}_2\text{@Cu-5}$ catalyst.

440 cm^{-1} changed on exposure to air. The above observations answer the two questions posed in the Introduction section as follows: (i) exposing the catalyst surface to air eliminates the defects due to re-oxidation and (ii) reducing conditions regenerate oxygen vacancies during repeated catalytic reactions.

4. Conclusions

We have synthesized metal-loaded TiO_2 catalysts by a solid-state method and shown the effects of interfacial oxygen vacancies on the catalytic efficiencies of the synthesized nanocatalysts. By analyzing the Raman spectra of various catalysts, we have shown that

the *in situ* formation of oxygen vacancies (TiO_{2-x}) during catalytic AB hydrolysis enhances the rate of the reaction. We have also identified the optimum catalytic formulation (M-3). The study also offers scope for exploring other synthetic strategies for an efficient metal–metal oxide interface and the use of other reducible oxides as supports in modulating the interfaces for the catalytic hydrolysis of AB and other such chemical transformations.

Author contributions

The manuscript was written through contributions of all authors. All authors have given approval to the final version



of the manuscript. This research did not receive any specific grant from funding agencies in the public, commercial, or not-for-profit sectors.

Data availability

The data supporting this article have been included as part of the ESI.†

Conflicts of interest

The authors declare no conflicts of interest.

Acknowledgements

DP would like to thank BITS-Pilani University for the fellowship. The instrumental facilities used at CAL facility in BITS-Pilani, Hyderabad Campus are gratefully acknowledged.

References

- 1 D. Maarisetty and S. S. Baral, Defect Engineering in Photocatalysis: Formation, Chemistry, Optoelectronics, and Interface Studies, *J. Mater. Chem. A*, 2020, **8**, 18560–18604.
- 2 Q. Yue, C. Liu, Y. Wan, X. Wu, X. Zhang and P. Du, Defect Engineering of Mesoporous Nickel Ferrite and Its Application for Highly Enhanced Water Oxidation Catalysis, *J. Catal.*, 2018, **358**, 1–7.
- 3 M. Shahrezaei, S. H. Hejazi, H. Kmentova, V. Sedajova, R. Zboril, A. Naldoni and S. Kment, Ultrasound-driven defect engineering in TiO_{2-x} nanotubes – toward highly efficient platinum single atom-enhanced photocatalytic water splitting, *ACS Appl. Mater. Interfaces*, 2023, **15**(31), 37976–37985.
- 4 E. Florez, P. Fuentealba and F. Mondragón, Chemical Reactivity of Oxygen Vacancies on the MgO Surface: Reactions with CO₂, NO₂ and Metals, *Catal. Today*, 2008, **133–135**, 216–222.
- 5 Q. Zhao, L. Fu, D. Jiang, J. Ouyang, Y. Hu, H. Yang and Y. Xi, Nanoclay-Modulated Oxygen Vacancies of Metal Oxide, *Commun. Chem.*, 2019, **2**, 1–10.
- 6 F. Esch, S. Fabris, L. Zhou, T. Montin, C. Africh, P. Fornasiero, G. Comelli and R. Rosei, Electron Localization Determines Defect Formation on Ceria Substrates, *Science*, 2005, **309**, 749–752.
- 7 B. B. Adormaa, W. K. Darkwah and Y. Ao, Oxygen Vacancies of the TiO₂ Nano-Based Composite Photocatalysts in Visible Light Responsive Photocatalysis, *RSC Adv.*, 2018, **8**, 33551–33563.
- 8 Y. Zhu, X. Liu, S. Jin, H. Chen, W. Lee, M. Liu and Y. Chen, Anionic Defect Engineering of Transition Metal Oxides for Oxygen Reduction and Evolution Reactions, *J. Mater. Chem. A*, 2019, **7**, 5875–5897.
- 9 G. Yin, X. Huang, T. Chen, W. Zhao, Q. Bi, J. Xu, Y. Han and F. Huang, Hydrogenated Blue Titania for Efficient Solar to Chemical Conversions: Preparation, Characterization, and Reaction Mechanism of CO₂ Reduction, *ACS Catal.*, 2018, **8**, 1009–1017.
- 10 S. Corby, L. Francàs, A. Kafizas and J. R. Durrant, Determining the Role of Oxygen Vacancies in the Photoelectrocatalytic Performance of WO₃ for Water Oxidation, *Chem. Sci.*, 2020, **11**, 2907–2914.
- 11 X. Pan, M. Q. Yang, X. Fu, N. Zhang and Y. J. Xu, Defective TiO₂ with Oxygen Vacancies: Synthesis, Properties and Photocatalytic Applications, *Nanoscale*, 2013, **5**, 3601–3614.
- 12 V. P. Indrakanti, J. D. Kubicki and H. H. Schobert, Photo-induced Activation of CO₂ on Ti-Based Heterogeneous Catalysts: Current State, Chemical Physics-Based Insights and Outlook, *Energy Environ. Sci.*, 2009, **2**, 745–758.
- 13 S. A. Rawool, K. K. Yadav and V. Polshettiwar, Defective TiO₂ for Photocatalytic CO₂ conversion to Fuels and Chemicals, *Chem. Sci.*, 2021, **12**, 4267–4299.
- 14 A. Sarkar and G. G. Khan, The Formation and Detection Techniques of Oxygen Vacancies in Titanium Oxide-Based Nanostructures, *Nanoscale*, 2019, **11**, 3414–3444.
- 15 X. Chen, L. Liu and F. Huang, Black Titanium Dioxide (TiO₂) Nanomaterials, *Chem. Soc. Rev.*, 2015, **44**, 1861–1885.
- 16 M. G. Ju, G. Sun, J. Wang, Q. Meng and W. Liang, Origin of High Photocatalytic Properties in the Mixed-Phase TiO₂: A First-Principles Theoretical Study, *ACS Appl. Mater. Interfaces*, 2014, **6**, 12885–12892.
- 17 P. Apopei, C. Catrinescu, C. Teodosiu and S. Royer, Mixed-Phase TiO₂ Photocatalysts: Crystalline Phase Isolation and Reconstruction, Characterization and Photocatalytic Activity in the Oxidation of 4-Chlorophenol from Aqueous Effluents, *Appl. Catal., B*, 2014, **160–161**, 374–382.
- 18 D. C. Hurum, A. G. Agrios, K. A. Gray, T. Rajh and M. C. Thurnauer, Explaining the Enhanced Photocatalytic Activity of Degussa P25 Mixed-Phase TiO₂ Using EPR, *J. Phys. Chem. B*, 2003, **107**, 4545–4549.
- 19 D. C. Hurum, A. G. Agrios, K. A. Gray, T. Rajh and M. C. Thurnauer, Explaining the Enhanced Photocatalytic Activity of Degussa P25 Mixed-Phase TiO₂ Using EPR, *J. Phys. Chem. B*, 2003, **107**, 4545–4549.
- 20 Q. Zhu, Y. Peng, L. Lin, C. M. Fan, G. Q. Gao, R. X. Wang and A. W. Xu, Stable Blue TiO_{2-x} Nanoparticles for Efficient Visible Light Photocatalysts, *J. Mater. Chem. A*, 2014, **2**, 4429–4437.
- 21 M. Zhang, Q. Pei, W. Chen, L. Liu, T. He and P. Chen, Room Temperature Synthesis of Reduced TiO₂ and Its Application as a Support for Catalytic Hydrogenation, *RSC Adv.*, 2017, **7**, 4306–4311.
- 22 H. Tan, Z. Zhao, M. Niu, C. Mao, D. Cao, D. Cheng, P. Feng and Z. Sun, A Facile and Versatile Method for Preparation of Colored TiO₂ with Enhanced Solar-Driven Photocatalytic Activity, *Nanoscale*, 2014, **6**, 10216–10223.
- 23 X. Ma, Y. Shi, Z. Cheng, X. Liu, J. Liu, Z. Guo, X. Cui, X. Sun, J. Zhao, S. Tan and B. Wang, Unveiling diverse coordination-defined electronic structures of reconstructed anatase TiO₂ (001)-(1 × 4) surface, *Nat. Commun.*, 2024, **15**(1), 2326.
- 24 S. V. Badalov, A. Bocchini, R. Wilhelm, A. L. Kozub, U. Gerstmann and W. G. Schmidt, Rutile, anatase, brookite



- and titania thin film from Hubbard corrected and hybrid DFT, *Mater. Res. Express*, 2023, **10**(7), 075501.
- 25 S. V. Badalov, R. Wilhelm and W. G. Schmidt, Photocatalytic properties of graphene-supported titania clusters from density-functional theory, *J. Comput. Chem.*, 2020, **41**(21), 1921–1930.
 - 26 K. Lau, B. Giera, S. Barcikowski and S. Reichenberger, The multivariate interaction between Au and TiO₂ colloids: the role of surface potential, concentration, and defects, *Nanoscale*, 2024, **16**(5), 2552–2564.
 - 27 H. Tang, Y. Su, B. Zhang, A. F. Lee, M. A. Isaacs, K. Wilson, L. Li, Y. Ren, J. Huang, M. Haruta, B. Qiao, X. Liu, C. Jin, D. Su, J. Wang and T. Zhang, Classical Strong Metal-Support Interactions between Gold Nanoparticles and Titanium Dioxide, *Sci. Adv.*, 2017, **3**, 1700231.
 - 28 T. S. Rajaraman, S. P. Parikh and V. G. Gandhi, Black TiO₂: A Review of Its Properties and Conflicting Trends, *Chem. Eng. J.*, 2020, **389**, 123918.
 - 29 Y. Xu, C. Zhang, L. Zhang, X. Zhang, H. Yao and J. Shi, Pd-Catalyzed Instant Hydrogenation of TiO₂ with Enhanced Photocatalytic Performance, *Energy Environ. Sci.*, 2016, **9**, 2410–2417.
 - 30 H. Bao, S. Zhu, L. Zhou, H. Fu, H. Zhang and W. Cai, Mars-van-Krevelen Mechanism-Based Blackening of Nano-Sized White Semiconducting Oxides for Synergetic Solar Photo-Thermocatalytic Degradation of Dye Pollutants, *Nanoscale*, 2020, **12**, 4030–4039.
 - 31 D. Ariyanti, L. Mills, J. Dong, Y. Yao and W. Gao, NaBH₄ Modified TiO₂: Defect Site Enhancement Related to Its Photocatalytic Activity, *Mater. Chem. Phys.*, 2017, **199**, 571–576.
 - 32 A. Naldoni, M. Altomare, G. Zoppellaro, N. Liu, Š. Kment, R. Zbořil and P. Schmuki, Photocatalysis with Reduced TiO₂: From Black TiO₂ to Cocatalyst-Free Hydrogen Production, *ACS Catal.*, 2019, **9**, 345–364.
 - 33 K. Zhang and J. H. Park, Surface Localization of Defects in Black TiO₂: Enhancing Photoactivity or Reactivity, *J. Phys. Chem. Lett.*, 2017, **8**, 199–207.
 - 34 X. Zhou, E. Wierzbicka, N. Liu and P. Schmuki, Black and White Anatase, Rutile and Mixed Forms: Band-Edges and Photocatalytic Activity, *Chem. Commun.*, 2019, **55**, 533–536.
 - 35 M. Kong, Y. Li, X. Chen, T. Tian, P. Fang, F. Zheng and X. Zhao, Tuning the Relative Concentration Ratio of Bulk Defects to Surface Defects in TiO₂ Nanocrystals Leads to High Photocatalytic Efficiency, *J. Am. Chem. Soc.*, 2011, **133**, 16414–16417.
 - 36 A. Naldoni, M. Allieta, S. Santangelo, M. Marelli, F. Fabbri, S. Cappelli, C. L. Bianchi, R. Psaro and V. Dal Santo, Effect of Nature and Location of Defects on Bandgap Narrowing in Black TiO₂ Nanoparticles, *J. Am. Chem. Soc.*, 2012, **134**, 7600–7603.
 - 37 A. R. Puigdollers, P. Schlexer, S. Tosoni and G. Pacchioni, Increasing Oxide Reducibility: The Role of Metal/Oxide Interfaces in the Formation of Oxygen Vacancies, *ACS Catal.*, 2017, **7**, 6493–6513.
 - 38 H. Chen, Z. Yang, X. Wang, F. Polo-Garzon, P. W. Halstenberg, T. Wang, X. Suo, S. Z. Yang, H. M. Meyer, Z. Wu and S. Dai, Photoinduced Strong Metal-Support Interaction for Enhanced Catalysis, *J. Am. Chem. Soc.*, 2021, **143**, 8521–8526.
 - 39 N. Tiwale, A. Subramanian, Z. Dai, S. Sikder, J. T. Sadowski and C. Y. Nam, Large mobility modulation in ultrathin amorphous titanium oxide transistors, *Commun. Mater.*, 2020, **1**(1), 94.
 - 40 A. Staubitz, A. P. M. Robertson and I. Mannes, Ammonia-Borane and Related Compounds as Dihydrogen Sources, *Chem. Rev.*, 2010, **110**, 4079–4124.
 - 41 C. Yüksel Alpaydın, S. K. Gülbay and C. Ozgur Colpan, A Review on the Catalysts Used for Hydrogen Production from Ammonia Borane, *Int. J. Hydrogen Energy*, 2020, **45**, 3414–3434.
 - 42 C. Wang and D. Astruc, Recent Developments of Nanocatalyzed Liquid-Phase Hydrogen Generation, *Chem. Soc. Rev.*, 2021, **50**, 3437–3484.
 - 43 S. Özkar, Magnetically Separable Transition Metal Nanoparticles as Catalysts in Hydrogen Generation from the Hydrolysis of Ammonia Borane, *Int. J. Hydrogen Energy*, 2021, **46**, 21383–21400.
 - 44 M. Zahmakiran and S. Özkar, Transition Metal Nanoparticles in Catalysis for the Hydrogen Generation from the Hydrolysis of Ammonia-Borane, *Top. Catal.*, 2013, **56**, 1171–1183.
 - 45 J. Liu, B. Li, Y. Dong, Q. Liu, Y. Song, Y. Guo, Y. Zhao, X. Li and J. Xiong, Hydrolysis of ammonia borane for hydrogen generation on bimetallic CoCu catalysts: regulation of synergistic effect, *Catal. Lett.*, 2024, **154**(2), 461–472.
 - 46 P. V. Ramachandran and P. D. Gagare, Preparation of Ammonia Borane in High Yield and Purity, Methanolysis, and Regeneration, *Inorg. Chem.*, 2007, **46**, 7810–7817.
 - 47 G. N. Glavee, K. J. Klabunde, C. M. Sorensen and G. C. Hadjapanayis, Borohydride Reductions of Metal Ions. A New Understanding of the Chemistry Leading to Nano-scale Particles of Metals, Borides, and Metal Borates, *Langmuir*, 1992, **8**, 771–773.
 - 48 S. A. Kondrat, G. Shaw, S. J. Freakley, Q. He, J. Hampton, J. K. Edwards, P. J. Miedziak, T. E. Davies, A. F. Carley, S. H. Taylor, C. J. Kiely and G. J. Hutchings, Physical Mixing of Metal Acetates: A Simple, Scalable Method to Produce Active Chloride Free Bimetallic Catalysts, *Chem. Sci.*, 2012, **3**, 2965–2971.
 - 49 T. U. B. Rao, B. Nataraju and T. Pradeep, Ag₉ Quantum Cluster through a Solid-State Route, *J. Am. Chem. Soc.*, 2010, **132**, 16304–16307.
 - 50 U. Sanyal, S. B. Kalidindi, S. Nair and B. R. Jagirdar, Towards Sustainability: A New, Solid-State Synthetic Route for Supported Metal Nanocatalysts, *Curr. Sci.*, 2012, **102**, 78–84.
 - 51 S. R. Nalluri, R. Nagarjuna, D. Patra, R. Ganesan and G. Balaji, Large Scale Solid-State Synthesis of Catalytically Active Fe₃O₄@M (M = Au, Ag and Au-Ag Alloy) Core-Shell Nanostructures, *Sci. Rep.*, 2019, **9**, 1–11.
 - 52 H. Tian, X. L. Zhang, J. Scott, C. Ng and R. Amal, TiO₂-Supported Copper Nanoparticles Prepared via Ion Exchange for Photocatalytic Hydrogen Production, *J. Mater. Chem. A*, 2014, **2**, 6432–6438.



- 53 H. L. Jiang and Q. Xu, Catalytic Hydrolysis of Ammonia Borane for Chemical Hydrogen Storage, *Catal. Today*, 2011, **170**, 56–63.
- 54 J. Li, Q. L. Zhu and Q. Xu, Non-Noble Bimetallic CuCo Nanoparticles Encapsulated in the Pores of Metal-Organic Frameworks: Synergetic Catalysis in the Hydrolysis of Ammonia Borane for Hydrogen Generation, *Catal. Sci. Technol.*, 2015, **5**, 525–530.
- 55 H. Wang, L. Zhou, M. Han, Z. Tao, F. Cheng and J. Chen, CuCo Nanoparticles Supported on Hierarchically Porous Carbon as Catalysts for Hydrolysis of Ammonia Borane, *J. Alloys Compd.*, 2015, **651**, 382–388.
- 56 H. Zhang, X. Gu, P. Liu, J. Song, J. Cheng and H. Su, Highly Efficient Visible-Light-Driven Catalytic Hydrogen Evolution from Ammonia Borane Using Non-Precious Metal Nanoparticles Supported by Graphitic Carbon Nitride, *J. Mater. Chem. A*, 2017, **5**, 2288–2296.
- 57 F. Z. Song, Q. L. Zhu, X. C. Yang and Q. Xu, Monodispersed CuCo Nanoparticles Supported on Diamine-Functionalized Graphene as a Non-Noble Metal Catalyst for Hydrolytic Dehydrogenation of Ammonia Borane, *ChemNanoMat*, 2016, **2**, 942–945.
- 58 S. Kim, Y. Cho, R. Rhee and J. H. Park, Black TiO₂: What Are Exact Functions of Disorder Layer, *Carbon Energy*, 2020, **2**, 44–53.
- 59 Y. Liu, P. Deng, R. Wu, X. Zhang, C. Sun and H. Li, Oxygen Vacancies for Promoting the Electrochemical Nitrogen Reduction Reaction, *J. Mater. Chem. A*, 2021, **9**, 6694–6709.
- 60 S. C. Yang, S. H. Pang, T. P. Sulmonetti, W. N. Su, J. F. Lee, B. J. Hwang and C. W. Jones, Synergy between Ceria Oxygen Vacancies and Cu Nanoparticles Facilitates the Catalytic Conversion of CO₂ to CO under Mild Conditions, *ACS Catal.*, 2018, **8**, 12056–12066.
- 61 J. Vecchiotti, A. Bonivardi, W. Xu, D. Stacchiola, J. J. Delgado, M. Calatayud and S. E. Collins, Understanding the Role of Oxygen Vacancies in the Water Gas Shift Reaction on Ceria-Supported Platinum Catalysts, *ACS Catal.*, 2014, **4**, 2088–2096.
- 62 O. Frank, M. Zukalova, B. Laskova, J. Kürti, J. Koltai and L. Kavan, Raman Spectra of Titanium Dioxide (Anatase, Rutile) with Identified Oxygen Isotopes (16, 17, 18), *Phys. Chem. Chem. Phys.*, 2012, **14**, 14567–14572.
- 63 Z. Zheng, B. Huang, J. Lu, Z. Wang, X. Qin, X. Zhang, Y. Dai and M. H. Whangbo, Hydrogenated Titania: Synergy of Surface Modification and Morphology Improvement for Enhanced Photocatalytic Activity, *Chem. Commun.*, 2012, **48**, 5733–5735.
- 64 L. W. Zhang, H. B. Fu and Y. F. Zhu, Efficient TiO₂ Photocatalysts from Surface Hybridization of TiO₂ Particles with Graphite-like Carbon, *Adv. Funct. Mater.*, 2008, **18**, 2180–2189.
- 65 A. Bulut, M. Yurderi, I. E. Ertas, M. Celebi, M. Kaya and M. Zahmakiran, Carbon Dispersed Copper-Cobalt Alloy Nanoparticles: A Cost-Effective Heterogeneous Catalyst with Exceptional Performance in the Hydrolytic Dehydrogenation of Ammonia-Borane, *Appl. Catal., B*, 2016, **180**, 121–129.
- 66 K. Feng, J. Zhong, B. Zhao, H. Zhang, L. Xu, X. Sun and S.-T. Lee, Cu_xCo_{1-x}O Nanoparticles on Graphene Oxide as A Synergistic Catalyst for High-Efficiency Hydrolysis of Ammonia-Borane, *Angew. Chem., Int. Ed.*, 2016, **128**, 12129–12133.
- 67 Z. H. Lu, J. Li, G. Feng, Q. Yao, F. Zhang, R. Zhou, D. Tao, X. Chen and Z. Yu, Synergistic Catalysis of MCM-41 Immobilized Cu-Ni Nanoparticles in Hydrolytic Dehydrogenation of Ammonia Borane, *Int. J. Hydrogen Energy*, 2014, **39**, 13389–13395.
- 68 W. Sang, C. Wang, X. Zhang, X. Yu, C. Yu, J. Zhao, X. Wang, X. Yang and L. Li, Dendritic Co_{0.52}Cu_{0.48} and Ni_{0.19}Cu_{0.81} Alloys as Hydrogen Generation Catalysts via Hydrolysis of Ammonia Borane, *Int. J. Hydrogen Energy*, 2017, **42**, 30691–30703.
- 69 F. Z. Song, Q. L. Zhu, X. C. Yang and Q. Xu, Monodispersed CuCo Nanoparticles Supported on Diamine-Functionalized Graphene as a Non-Noble Metal Catalyst for Hydrolytic Dehydrogenation of Ammonia Borane, *ChemNanoMat*, 2016, **2**, 942–945.
- 70 J. M. Yan, Z. L. Wang, H. L. Wang and Q. Jiang, Rapid and Energy-Efficient Synthesis of a Graphene-CuCo Hybrid as a High Performance Catalyst, *J. Mater. Chem.*, 2012, **22**, 10990–10993.
- 71 C. Li, J. Zhou, W. Gao, J. Zhao, J. Liu, Y. Zhao, M. Wei, D. G. Evans and X. Duan, Binary Cu–Co Catalysts Derived from Hydrotalcites with Excellent Activity and Recyclability towards NH₃BH₃ Dehydrogenation, *J. Mater. Chem. A*, 2013, **1**, 5370–5376.
- 72 J. Song, X. Gu, Y. Cao and H. Zhang, Porous Oxygen Vacancy-Rich V₂O₅ Nanosheets as Superior Semiconducting Supports of Nonprecious Metal Nanoparticles for Efficient on-Demand H₂ Evolution from Ammonia Borane under Visible Light Irradiation, *J. Mater. Chem. A*, 2019, **7**(17), 10543–10551.
- 73 J. Song, F. Wu, Y. Lu, X. Zhang and Z. Li, CeVO₄/CeO₂ Heterostructure-Supported Co Nanoparticles for Photocatalytic H₂ Production from Ammonia Borane under Visible Light, *ACS Appl. Nano Mater.*, 2021, **4**, 4800–4809.
- 74 S. Zhou, Y. Yang, P. Yin, Z. Ren, L. Wang and M. Wei, Metal-Support Synergistic Catalysis in Pt/MoO_{3-x} Nanorods toward Ammonia Borane Hydrolysis with Efficient Hydrogen Generation, *ACS Appl. Mater. Interfaces*, 2022, **14**, 5275–5286.
- 75 S. Guan, L. An, S. Ashraf, L. Zhang, B. Liu, Y. Fan and B. Li, Oxygen Vacancy Excites Co₃O₄ Nanocrystals Embedded into Carbon Nitride for Accelerated Hydrogen Generation, *Appl. Catal., B*, 2020, **269**, 118775.

